Mapping sub-pixel surface roughness on Mars using high-resolution satellite image data

Amit Mushkin[1] and Alan R. Gillespie[1]

[1] The ratio between co-registered pixels in stereo or repeat image pairs is used to constrain the deviation of the Martian surface from Lambertian reflection due to unresolved shadows at the pixel scale of orbiting imagers. Relative differences between the ratios primarily reflect differences in the effective amount of shadows 'seen' by the sensor in the two measurements, and are thus used as a relative proxy for sub-pixel surface roughness (SR). In-scene atmospheric corrections enable simple application of this 'two-look' approach, which facilitates robust SR mapping at spatial resolutions comparable to the image data. Relative 'two-look' SR estimates can be translated to physical SR parameters through empirical calibration using ground-based measurements. SR variation maps in Gusev crater were derived from THEMIS and HRSC images at 18- and 30- m/pixel, respectively. The latter were calibrated using measurements from Spirit to produce a quantitative clast-coverage map of Spirit's initial traverse in Gusev crater. **Citation:** Mushkin, A., and A. R. Gillespie (2006), Mapping sub-pixel surface roughness on Mars using high-resolution satellite image data, *Geophys. Res. Lett.*, *33*, L18204, doi:10.1029/2006GL027095.

1. Introduction

[2] Surface roughness (SR) is regarded here as the unresolved topographic expression of the surface, integrated over all length scales below the resolution of available digital elevation models (DEM's). SR is widely recognized as a fundamental variable for many aspects of Mars research such as future landing-site selection [e.g., *Golombek et al.*, 2003], geologic and geomorphologic studies [e.g., *Martinez-Alonso et al.*, 2005] and spectral analysis of the Martian surface [e.g., *Adams et al.*, 1986; *Cord et al.*, 2005; *Shkuratov et al.*, 2005].

[3] Previous studies estimated SR on Mars at spatial resolutions $>10^2$ m/pixel using radar returns [e.g., *Simpson et al.*, 1992; *Nouvel et al.*, 2006], thermal inertia [e.g., *Jakosky*, 1979; *Christensen et al.*, 2005; *Fergason et al.*, 2006], Mars Orbital Laser Altimeter (MOLA) pulse width [e.g., *Neumann et al.*, 2003], and extraction of Hapke and other roughness parameters from multi-angular optical data [e.g., *Pinet et al.*, 2005]. High-resolution ($<10^1$ m) local DEM's (i.e., supra-pixel roughness) derived from Mars Orbital Camera (MOC) data through stereogrammetry and photoclinometry methods [*Kirk et al.*, 2003; *Beyer et al.*, 2003] were used to improve the separation between effects of surface composition and SR at the $<10^2$ m/pixel scales. Yet, ground-based data from the Mars landers [e.g., *Golombek et al.*, 2006] confirm that, as observed on Earth [e.g., *Weeks et al.*, 1996], SR is variable at sub-pixel scales and a synthesis of multiple approaches is required to reduce ambiguities in its estimation [*Golombek et al.*, 2003].

[4] The 'two-look' approach we present in this paper was developed and established as a quantitative tool for remote geomorphic investigations of unvegetated surfaces on Earth [*Mushkin and Gillespie*, 2005]. The approach relies on the correlation between SR and the amount of shadows on the surface, which we constrain using the difference in apparent darkening or lightening of surfaces due to unresolved shadows between two co-registered images acquired at different illumination or viewing geometries, i.e., deviation from Lambertian reflection (Figure 1). Here, we discuss the modification of this approach for Mars and demonstrate its application as a simple and robust tool for mapping SR using Mars Express (MEx) High Resolution Stereo Camera (HRSC) images or repeat Thermal Emission Imaging System (THEMIS) visible images.

2. Approach

[5] Orbital measurements of visible to near-infrared radiance (L_{sensor}) reflected from the surface of Mars can be described by:

$$L_{(sensor)} = \frac{1}{\pi}\left(I\tau_{(sun)} + S_{\downarrow}\right)\rho\tau_{(sensor)}(1 - f_{sh}) + \frac{1}{\pi}S_{\downarrow}\rho\tau_{(sensor)}f_{sh} + S^{\uparrow} \quad (1)$$

where I is solar irradiation at top of atmosphere, $\tau_{(sun)}$ and $\tau_{(sensor)}$ are atmospheric transmissivity in the sun- and sensor-surface paths, respectively, ρ is surface reflectivity if it were perfectly smooth, $S_{\downarrow}$ is down-welling sky irradiance and $S^{\uparrow}$ is up-welling path radiance. Parameter f_{sh} is the effective fraction of the pixel area that is in shadows, which for a given pixel varies with solar incidence angle (i) and sensor view angle (θ) (Figure 1). Equation 1 can be re-arranged so that:

$$L_{(sensor)} = \frac{1}{\pi}I\tau_{(sun)}\tau_{(sensor)}\rho(1 - f_{sh}) + \underbrace{\frac{1}{\pi}S_{\downarrow}\rho\tau_{(sensor)} + S^{\uparrow}}_{C} \quad (2)$$

where the last two terms, grouped together as C represent $L_{(sensor)}$ of a completely shadowed pixel, for which $f_{sh} = 1$. Thus, resolved shadows in the scene can be used to remove C from equation 2 and the ratio $L_{(sensor)1}/L_{(sensor)2}$ between co-registered pixels in images acquired at two different

[1]Department of Earth and Space Sciences, University of Washington, Seattle, Washington, USA.
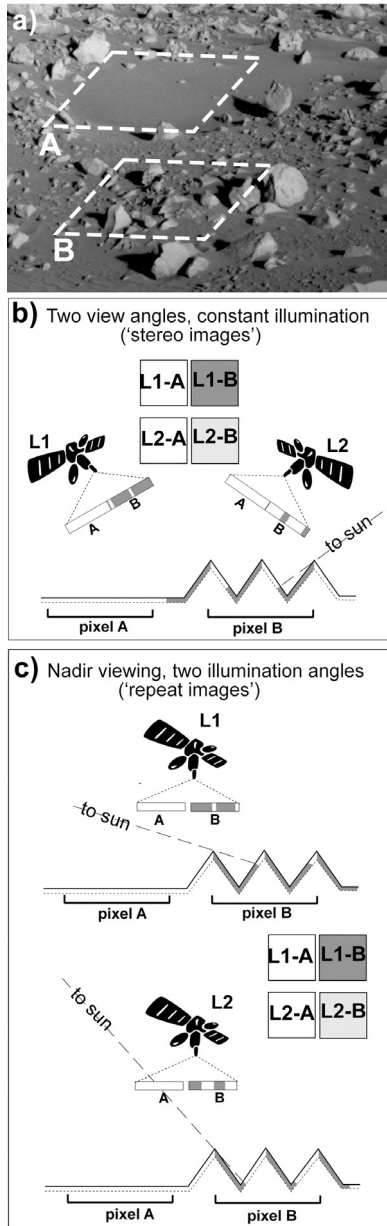
Figure 1. The 'two-look' approach for mapping sub-pixel surface roughness. (a) Subset of Spirit Pancam image 2P136234337EFF3600P2401R1M1 on sol 111 (http://marsrovers.jpl.nasa.gov/gallery/all/2/p/). Fewer shadows are cast in smooth 'pixel A' than in rough 'pixel B'. Image is ~1 m across. (b) The difference in surface lightness viewed from different angles, but the same illumination angle is related to the amount of sub-pixel shadowing and roughness. Shadows in pixel B that are not visible to the sensor from L2 become visible from L1; the integrated result over a pixel area will be darkening of L1-B relative to L2-B. Area A has few shadows and therefore no lightness difference will be observed between L1-A and L2-A. (c) Same concept as Figure 1b, only here illumination angle changes and view angle remains the same.

illumination conditions (repeat images) or at two different view angles (stereo images) becomes:

$$\frac{L_{(sensor)1}}{L_{(sensor)2}} = \frac{\frac{1}{\pi}I_1\tau_{(sun)1}\tau_{(sensor)1}\rho_1(1 - f_{sh1})}{\frac{1}{\pi}I_2\tau_{(sun)2}\tau_{(sensor)2}\rho_2(1 - f_{sh2})} \qquad (3)$$

This system is inherently under-determined as it comprises two measurements and ten unknowns. However, if no compositional change occurs on the surface between the two measurements (i.e., $\rho_1 = \rho_2$) and I, $\tau_{(sun)}$ and $\tau_{(sensor)}$ remain constant, e.g., similarly sloping co-registered pixels within a given image for which atmospheric conditions, i and θ are the same, Equation 3 can be reduced to:

$$\frac{L_{(sensor)1}}{L_{(sensor)2}} = k_I k_\tau \frac{(1 - f_{sh1})}{(1 - f_{sh2})} \qquad (4)$$

where $k_I = {I_1\tau_{(sun)1}}/{I_2\tau_{(sun)2}}$ and $k_\tau = {\tau_{(sensor)1}}/{I_2\tau_{(sensor)2}}$. Although k_I and k_τ are unknown, they remain constant across the scene for similarly sloping pixels in the two images. Thus, pixel-to-pixel variations in $L_{(sensor)1}/L_{(sensor)2}$ are theoretically independent of ρ, and primarily reflect differences between f_{sh1} and f_{sh2} (i.e., Δf_{sh}). Perfectly smooth Lambertian surfaces are expected to yield $L_{(sensor)1}/L_{(sensor)2} = k_I k_\tau$ (f_{sh} = 0 at all angles → $\Delta f_{sh} = 0$) and increasingly rough, disordered surfaces yield diverging $L_{(sensor)1}/L_{(sensor)2}$ values as Δf_{sh} increases with surface roughness [*Mushkin and Gillespie*, 2005]. The sign of this divergence can be readily determined from the general viewing and illumination geometries (Figure 1), and thus $L_{(sensor)1}/L_{(sensor)2}$ can be used as a proxy for mapping Δf_{sh} and relative sub-pixel *SR* variations without the need to determine the constants in Equation 4 explicitly. Empirical calibrations against ground measurements or model-based radiosity predictions facilitate inversion of $L_{(sensor)1}/L_{(sensor)2}$ values for actual physical *SR* parameters.

[6] As described above, the 'two-look' approach requires a set of two or more overlapping images acquired at different illumination and/or viewing geometries. At present, such high-resolution image data for Mars are available from HRSC [*Neukum et al.*, 2004], THEMIS [*Christensen et al.*, 2004] and MOC [*Malin et al.*, 1992]. These data represent three different variants of the 'two-look' approach: HRSC offers stereo image data (>25 m/pixel) acquired at the same time and illumination conditions, but at different view angles (i.e., $i_1 \approx i_2$ and $\theta_1 \neq \theta_2$); THEMIS offers repeat images (>18 m/pixel) acquired at different times and illumination conditions, but typically at nearly the same nadir view angle (i.e., $i_1 \neq i_2$ and $\theta_1 \approx \theta_2$); and MOC offers repeat images (>1.5 m/pixel) typically acquired at different illumination conditions as well as view angles (i.e., $i_1 \neq i_2$ and $\theta_1 \neq \theta_2$).

[7] The unique data acquisition configuration of the HRSC experiment [*Neukum et al.*, 2004] comprises nine linear array detectors oriented perpendicular to the ~N-S orbit track. They view the surface at different angles spread out from 18.9° forward to 18.9° aft of nadir so that each detector views a different line in the scene at any instant, where lag time between acquisition of overlapping stereo lines is typically <1 min. Though field of view for one pixel at nadir and 250 km orbit altitude is nominally 10 m

(40 μrad), stereo images are typically acquired in the macro-pixel mode, in which pixels are aggregated and yield effective pixel footprints ranging from ~25 to 500 m. We utilize outer stereo channels S1 and S2 ($\theta_{1,2} = \pm 18.9°$) to maximize Δf_{sh} and the detectability of *SR* variations.

3. Results

[8] *SR* variations at Gusev crater were mapped using: a) HRSC Level-2 data (Orbit 24) from stereo channels S1 and S2, and b) overlapping THEMIS visible images V00881003 and V07909002, acquired on 2/25/2002 and 9/26/2003, respectively. The HRSC images used were acquired at ~30 m/pixel resolution, solar elevation, solar azimuth and satellite track inclination at time of acquisition were 65°, 275° and 86.6°, respectively. This geometric configuration implies that the ratio $L_{(S2)}/L_{(S1)}$ is proportional to Δf_{sh} (Equation 3) and that higher $L_{(S2)}/L_{(S1)}$ values imply rougher surfaces. The two nadir THEMIS images used were acquired at ~18 m/pixel resolution. Solar elevation and azimuths at time of acquisitions were 45.8° and 266.2°, respectively, for image V00881003, and 23.3° and 245.6°, respectively, for image V07909002. For this configuration of THEMIS images the ratio $L_{(V00881003)}/L_{(V07909002)}$ is expected to be proportional to Δf_{sh} (Equation 3) with higher $L_{(V00881003)}/L_{(V07909002)}$ values implying rougher surfaces. In both cases, uncertainties in ratio values due to signal-to-noise ratio (*snr*) are estimated at <1.4%. Uncertainties due atmospheric corrections are analyzed in the discussion section below.

[9] As shown in Figure 2, the two independent HRSC- and THEMIS-derived *SR* maps display generally similar patterns, excluding notable discrepancies in the southwest corner of the mapped area and along the Spirit's traverse between Missoula and Lahontan craters, where anomalously high *SR* values were mapped from the THEMIS data. THEMIS-derived roughness estimates appear to display a SE-NW fabric. The high spatial resolution of both roughness maps allows for direct comparison with corresponding ground-based images such as those acquired by Spirit's Panoramic Camera [*Bell et al.*, 2003] along Spirit's traverse (Figures 2c−2f). Increasing *SR* from Spirit's landing point at 'Columbia Memorial Station' (CMS) through the ejecta blanket and to the rim of Bonneville crater (BC) was mapped with both data sets and is consistent with Spirit's ground observations [e.g., *Golombek et al.*, 2005] as well as with the THEMIS-derived thermal-inertia map [*Fergason et al.*, 2006] for the BC surroundings (not shown here). The lowest *SR* values in both maps occur in the floors of BC, MC and Lahontan crater (LC) where sandy, smooth and nearly rock-free surfaces were identified [*Grant et al.*, 2006; *Golombek et al.*, 2006]. Spirit traversed intercrater terrain between MC and its ejecta and LC (Figure 2f), which is smoother than ejecta-blanket terrain [*Golombek et al.*, 2006], and thus HRSC *SR* estimates appear more consistent with the ground-based observations.

4. Discussion

[10] We use ratio images between co-registered stereo or repeat data to obtain a proxy for relative *SR* variations on the surface of Mars. One of the most important limitations
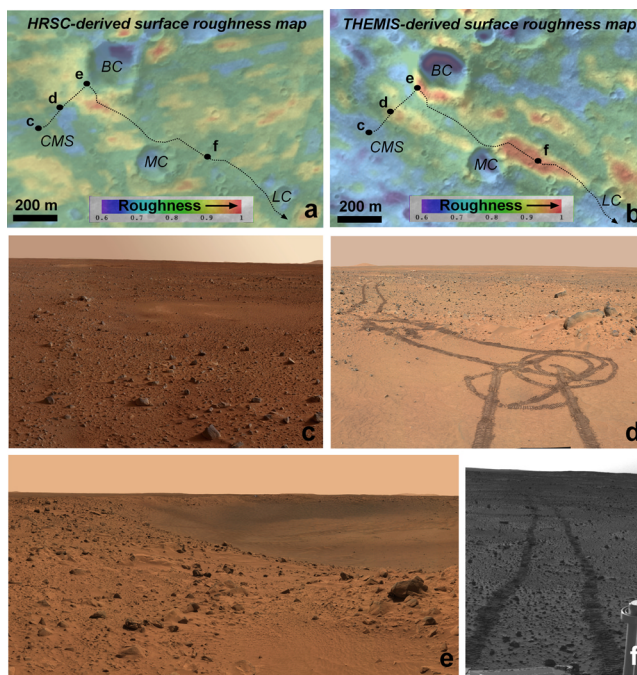

Figure 2. Relative roughness maps and rover views at Gusev crater. (a) HRSC at-sensor radiance ratio between co-registered S1 and S2 stereo images. The ~30-m/pixel data were re-sampled to the ~1.5-m/pixel resolution of the MOC mosaic (http://www.msss.com/mars_images/moc/2005/01/03/) on which they are superimposed. Dotted line represents the traverse of Spirit from its landing site at the Columbia Memorial Station (CMS) through Bonneville crater (BC), Missoula crater (MC), Lahontan crater (LC) and towards the Columbia Hills (not shown). North is up. (b) THEMIS ratio between two co-registered 'repeat' images. The ~18-m/pixel data were re-sampled and super-imposed on the same MOC image as in Figure 2a. (c, d, e) Subsets from Spirit's Pancam at CMS (Figure 2c), Legacy Station ~half way to BC (Figure 2d), and on the rim of BC (Figure 2e) in order of increasing roughness. Pancam images released 1/27/2004, 2/08/2005 and 3/15/2004, respectively (http://marsrovers.jpl.nasa.gov/). The sandy floor of BC is shown on the right side of Figure 2e. (f) Subset of mosaic from Spirit navigation camera (released 04/26/2004, http://marsrovers.jpl.nasa.gov/) showing the characteristic inter-crater terrain between MC ejecta blanket and LC.

of this approach is that *SR* estimates remain valid only for commonly illuminated surfaces within each of the images used, i.e., for 'similarly sloping' surfaces (Equations 3, 4). Numerical simulations suggest the effect of pixel slope on L_1/L_2 values is <9% for $\pm 5°$ slopes about horizontal and that sensitivity to slope increases significantly for steep gradients where the 9% criterion described above implies a smaller range of valid slopes.

[11] Another limitation of the 'two-look' approach arises from atmospheric corrections. Whereas atmospheric trans-missivity can be regarded as a constant scaling factor across the ratio image (i.e., k_τ in Equation 4), the contributions of both upwelling and down-welling atmospheric scattering to $L_{(sensor)}$, i.e., term *C* in equation 2, have to be accounted for.

To achieve this we employ an in-scene correction, in which the radiance value from a completely shadowed and re-solved area in the scene ('dark pixel') is subtracted from each of the images used. Whereas this correction is simple to apply, it is not trivial because C itself varies with albedo (Equation 2). The error associated with this 'dark pixel' correction (E_ρ) is proportional to the fraction of at-sensor radiance resulting from atmospheric scattering, i.e., $C/L_{(sensor)}$, as well as to the difference ($\Delta\rho^*$) between ρ of the pixel and ρ of the 'dark pixel' (ρ_{dp}) used. Negative $\Delta\rho^*$ values (i.e., $\rho < \rho_{dp}$) result in significantly larger E_ρ than corresponding positive $\Delta\rho^*$ values (Figure 3a), implying that $C(\rho_{dp})$ should be determined from the lowest-albedo surface possible, and that using $L_{(sensor)1}/L_{(sensor)2}$ as a proxy for SR may be problematic in cases where $\rho \ll \rho_{dp}$. Considering a scene with a range of typical non-ice albedo values on Mars, i.e., $0.05-0.3$, and $C(\rho_{dp})$ determined from a surface with a midrange albedo of 0.175, $E_\rho < 8\%$ requires that $C/L_{(sensor)} < 0.3$ (Figure 3b). For less favorable atmospheric conditions with larger $C/L_{(sensor)}$ values E_ρ can be significantly reduced if: 1) $C(\rho_{dp})$ is determined from a low-albedo surface, 2) a smaller range of albedo values can be a priori assumed for the scene or 3) low-albedo surfaces with $\rho_{dp} - \rho > 0.05$ are excluded from analysis (Figure 3b). Accordingly, E_ρ for the HRSC and THEMIS Gusev crater data used in Figures 2a and 2b are estimated at 7 and <1%, respectively, assuming the range of albedo values for the mapped area is 0.25 ± 0.05 [*Bell et al.*, 2004]. An additional source for uncertainties is the *snr* of the specific data used to produce the ratio images. For the common case in the visible wavelengths of *snr* > 100, the associated error is estimated at <1.4%. Image-to-image misregistration as well as image artifacts such as data compression or cross-talk between detectors may also degrade SR detectability and spatial resolution.

[12] The 'two-look' approach preserves the high spatial resolution of the image data used because only two images are used and registration errors are minimized. More complete characterization of the photometric function requires more "looks" and increases the opportunity for errors in atmospheric corrections as well as misregistration leading to potential reduction of useful resolution. In this regard, although MOC offers better spatial resolution than either HRSC or THEMIS, interpreting MOC-derived $L1/L2$ values in the context of SR variations in the scene appears to be significantly complicated by the variable viewing and illumination angles that are typical for MOC repeat images. We therefore focused in this paper on the simpler and more robust cases of THEMIS and HRSC data.

[13] Pixel resolution and area coverage of individual THEMIS and HRSC images are comparable, though at present, THEMIS offers a readily accessible global data base with good coverage of repeat images, whereas HRSC offers a less extensive data base for which public access at present is partially limited. The typical nadir viewing of THEMIS allows for relatively simple and parallax-free image-to-image registration, which reduces registration errors relative to oblique images. Nadir viewing also implies that Δf_{sh} from THEMIS data do not depend on the angle between the satellite orbit track and the solar principle plane – an important factor that can reduce SR detectability using
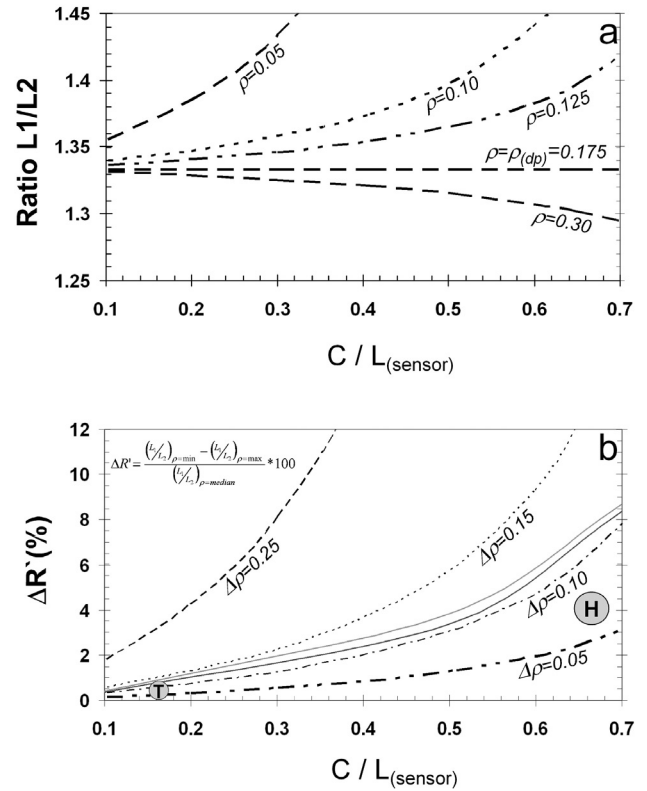

Figure 3. Numerical simulations showing the effect of atmospheric scattering on at-sensor radiance ratios for a given surface with $\Delta fsh = 20\%$ (a) $L1/L2$ as a function of $C/Lsensor$, where $Lsensor$ is measured radiance at the sensor and C is the contribution from atmospheric scattering defined in equation 2. ρ is surface albedo and $\rho_{(dp)}$ is surface albedo of the 'dark pixel' used to determine C. Deviations from a ratio of 1.333 are errors, which increase with $C/Lsensor$ and are asymmetrically skewed towards low albedo values. Typical range of HRSC $L1/L2$ values is $>\sim0.3$. (b) Error in $L1/L2$ as a function of $C/Lsensor$. $D\rho = r(\max) - \rho(\min)$ and curve-style corresponds to $\rho(\min)$ as curves in Figure 3a. Solid bright and dark gray lines depict albedo ranges of 0.25 and 0.15, respectively, that were reduced by excluding surfaces with $\rho - \rho dp > 0.05$ from the analysis. H, T represent HRSC and THEMIS data used in Figure 2, respectively.

HRSC data. For example, Δf_{sh} for a given surface and illumination conditions will be maximized when the HRSC satellite track is along the principle solar plane (Figure 1b) and will be reduced to $\Delta f_{sh} = 0$ when the satellite track is orthogonal to it, because in the latter case no 'shadow hiding' occurs between the two view angles and thus $f_{sh1} = f_{sh2}$.

[14] However, a predominant advantage of HRSC data over THEMIS data is the nearly simultaneous acquisition of the stereo images, which eliminates the possibility of change in surface albedo between the two measurements – a fundamental assumption of the 'two-look approach' (Equation 3). *Greeley et al.* [2005] identified local albedo changes as well as formation of dark wind streaks at Gusev crater over relatively short time scales of 20 sols and $\sim$5 months, respectively. Consequently, the discrepancies

between the HRSC- and THEMIS-derived roughness maps produced for Gusev crater (Figure 2) may be related to such albedo changes on the surface between acquisition times of the two THEMIS images used. The erroneously high SR mapped along the MC-LS segment of Spirit's traverse using THEMIS data is consistent with the formation of a dark wind streak along this segment between 2/2002 and 9/2003 and also has the same general southeast orientation identified for many dark streaks in this area [*Greeley et al.*, 2006], which also align with the SE-NW fabric of the THEMIS-derived SR map. Such rapid albedo changes are attributed to aeolian activity resulting in dust removal and deposition [*Greeley et al.*, 2005], which are regarded as ubiquitous on the Martian surface. The L_1/L_2 ratio derived from HRSC stereo images therefore appears to be a more robust proxy for SR variations than that obtained from repeat THEMIS data, although the latter are more widely available at present.

[15] Calibration is required to translate the L_1/L_2 ratio used in the 'two-look' approach into a physically meaningful roughness parameter. Such calibration can be achieved by matching measured L_1/L_2 values to model-based radiosity predictions for synthetic surfaces or for more realistic analog surfaces on Earth, which can now be readily characterized at the mm scale using ground-based laser scanners. In this regard, HRSC data have an additional advantage over THEMIS data in that the surface-sensor optical path length remains the same at both HRSC view angles because they are acquired nearly simultaneously and at fixed angles of ±18.9°, whereas THEMIS looks through the changing Martian atmosphere at different times. Thus, atmospheric transmissivity for HRSC is the same in both stereo images and does not have to be accounted for when using HRSC stereo data.

[16] Empirical calibration of 'two-look' L_1/L_2 ratios against ground-based roughness measurements obtained from the Mars Exploration rovers is feasible because the spatial resolution of the two data sets is typically comparable. Here, we constrain a calibration curve (Figure 4a) for the relative HRSC SR estimates in Figure 2a by using the rock size-frequency distribution estimates reported by *Golombek et al.* [2005] for selected locations along Sprit's traverse, ranging in area from 56.9 to 84.1 m^2. Measurement errors for the HRSC $L1/L2$ ratio are <1.4% and errors related to co-registration and scaling between measurement area and pixel footprint are ignored. The non-linear regression (linear on a semi-log field) we calculated, implies that extrapolations beyond the range of roughness values in Figure 4a may be problematic. The map of rock size-frequency distribution in the vicinity of Sprit's landing site and traverse (Figure 4b) shows that the roughest surfaces in this part of Gusev crater are consistent with the a 25−35% rock abundance and do not necessarily occur as continuous ejecta blankets around large craters.

[17] The 'two-look' approach complements other methods of remotely estimating high-resolution SR on Mars. It can be used in concert with THEMIS thermal inertia (TI) mapping [e.g., *Fergason et al.*, 2006] to help constrain the effects of bulk properties vs. SR on the TI estimates, and in concert with high-resolution photoclinometry methods [e.g., *Beyer et al.*, 2003] to distinguish between albedo and SR variations. Other studies successfully demonstrated the use
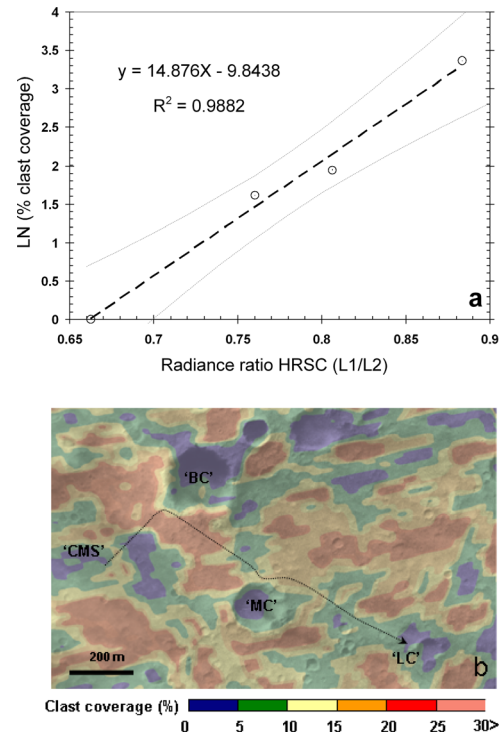

Figure 4. Calibrated roughnesses. (a) Calibration of HRSC-derived relative-roughness estimates to % rock abundance as estimated by *Golombek et al.* [2005] for locations c, d, and e in Figure 2a. An additional point from the relatively rock-free (assumed 1% rock abundance), sandy floor of BC (Figure 2e) was added to the calibration curve. Dotted lines represent the 1-sigma error bounds associated with this regression. (b) Calibrated roughness levels (as % rock abundance) using curve from Figure 4a and the data presented in Figure 2a. Dotted line represents approximate traverse of Spirit and lettering is the same as in Figure 2.

of HRSC multi-angular and multi-temporal data to map SR by extracting measures such as the Hapke photometric and roughness parameters [e.g., *Pinet et al.*, 2006]. The 'two-look' approach we present here complements these studies because the relative SR estimates we obtain are largely independent of surface composition, allow for independent in-scene atmospheric corrections, and are simple to derive at <~2-pixel spatial resolution from a single pair of co-registered stereo or repeat images.

5. Summary and Conclusions

[18] The 'two-look' approach utilizes the deviation from Lambertian reflection observed for rough surfaces on Mars at the pixel-scale of orbiting imagers, and offers a simple and robust tool for mapping sub-pixel surface roughness variations using HRSC stereo (>25 m/pixel) or THEMIS repeat images (>18 m/pixel). 'Two-look' SR estimates: 1) offer high spatial resolution that is comparable to that of the image data used, 2) require only a simple 'in-scene' compensation for atmospheric scattering, which is valid for typical Martian conditions as long as $C/L_{sensor} < 0.7$ and 3) are largely independent of atmospheric transmissivity

and surface albedo. Calibration of the 'two-look' relative *SR* estimates, whether using empirical data or model-based predictions, facilitates high-resolution quantitative mapping of sub-pixel surface roughness on Mars.

References

Adams, J. B., M. O. Smith, and P. E. Johnson (1986), Spectral mixture modeling: A new analysis of rock and soil types at the Viking Lander-1 site, *J. Geophys. Res.*, *91*, 8098–8112.

Bell, J. F., et al. (2003), Mars Exploration Rover Athena Panoramic Camera (Pancam) investigation, *J. Geophys. Res.*, *108*(E12), 8063, doi:10.1029/2003JE002070.

Bell, J. F., et al. (2004), Pancam multispectral imaging results from the Spirit Rover at Gusev crater, *Science*, *305*, 800–806.

Beyer, R. A., A. S. McEwen, and R. L. Kirk (2003), Meter-scale slopes of candidate MER landing sites from point photoclinometry, *J. Geophys. Res.*, *108*(E12), 8085, doi:10.1029/2003JE002120.

Christensen, P. R., et al. (2004), The Thermal Emission Imaging System (THEMIS) for the Mars 2001 Odyssey mission, *Space Sci. Rev.*, *110*, 85–130.

Christensen, P. R., et al. (2005), Mars Exploration Rover candidate landing sites as viewed by THEMIS, *Icarus*, *176*, 12–43.

Cord, A. M., et al. (2005), Experimental determination of the surface photometric contribution in the spectral reflectance deconvolution processes for a simulated Martian crater-like regolithic target, *Icarus*, *175*, 78–91.

Fergason, R. L., P. R. Christensen, J. F. Bell III, M. P. Golombek, K. E. Herkenhoff, and H. H. Kieffer (2006), Physical properties of the Mars Exploration Rover landing sites as inferred from Mini-TES-derived thermal inertia, *J. Geophys. Res.*, *111*, E02S21, doi:10.1029/2005JE002583.

Golombek, M. P., et al. (2003), Selection of the Mars Exploration Rover landing sites, *J. Geophys. Res.*, *108*(E12), 8072, doi:10.1029/2003JE002074.

Golombek, M. P., et al. (2005), Assessment of Mars Exploration Rover landing site predictions, *Nature*, *436*, 44–48.

Golombek, M. P., et al. (2006), Geology of the Gusev cratered plains from the Spirit rover transverse, *J. Geophys. Res.*, *111*, E02S07, doi:10.1029/2005JE002503.

Grant, J. A., et al. (2006), Crater gradation in Gusev crater and Meridiani Planum, Mars, *J. Geophys. Res.*, *111*, E02S08, doi:10.1029/2005JE002465.

Greeley, R., et al. (2005), Martian variable features: New insight from the Mars Express Orbiter and the Mars Exploration Rover Spirit, *J. Geophys. Res.*, *110*, E06002, doi:10.1029/2005JE002403.

Greeley, R., et al. (2006), Gusev crater: Wind-related features and processes observed by the Mars Exploration Rover Spirit, *J. Geophys. Res.*, *111*, E02S09, doi:10.1029/2005JE002491.

Jakosky, B. M. (1979), Effects of nonideal surfaces on the derived thermal-properties of Mars, *J. Geophys. Res.*, *84*, 8252–8262.

Kirk, R. L., E. Howington-Kraus, B. Redding, D. Galuszka, T. M. Hare, B. A. Archinal, L. A. Soderblom, and J. M. Barrett (2003), High-resolution topomapping of candidate MER landing sites with Mars Orbiter Camera narrow-angle images, *J. Geophys. Res.*, *108*(E12), 8088, doi:10.1029/2003JE002131.

Malin, M. C., G. E. Danielson, A. P. Ingersoll, H. Masursky, J. Veverka, M. A. Ravine, and T. A. Soulanille (1992), Mars Observer Camera, *J. Geophys. Res.*, *97*(E5), 7699–7718.

Martinez-Alonso, S., B. M. Jakosky, M. T. Mellon, and N. E. Putzig (2005), A volcanic interpretation of Gusev crater surface materials from thermophysical, spectral, and morphological evidence, *J. Geophys. Res.*, *110*, E01003, doi:10.1029/2004JE002327.

Mushkin, A., and A. R. Gillespie (2005), Estimating sub-pixel surface roughness using remotely sensed stereoscopic data, *Remote Sens. Environ.*, *99*, 75–83.

Neukum, G., et al. (2004), Recent and episodic volcanic and glacial activity on Mars revealed by the High Resolution Stereo Camera, *Nature*, *432*, 971–979.

Neumann, G. A., J. B. Abshire, O. Aharonson, J. B. Garvin, X. Sun, and M. T. Zuber (2003), Mars Orbiter Laser Altimeter pulse width measurements and footprint-scale roughness, *Geophys. Res. Lett.*, *30*(11), 1561, doi:10.1029/2003GL017048.

Nouvel, J. F., et al. (2006), Top layers charaterization of the Martian surface: Permittivity estimation based on geomorphology analysis, *Planet. Space Sci.*, *54*, 337–344.

Pinet, P. C., et al. (2005), Mars Express imaging photometry and surface geologic processes at Mars: What can be monitored within Gusev crater?, *Lunar Planet. Sci.*, *XXXVI*, abstract 1721.

Pinet, P. C., et al. (2006), Mars Express/HRSC imaging photometry and MER Spirit/Pancam in situ spectrophotometry within Gusev, *Lunar Planet. Sci.*, *XXXVII*, abstract 1220.

Shkuratov, Y. G., et al. (2005), Interpreting photometry of regolith-like surfaces with different topographies: Shadowing and multiple scattering, *Icarus*, *173*, 3–15.

Simpson, C. J., J. K. Harmon, S. H. Zisk, T. W. Thompson, and D. O. Muhleman (1992), Radar determination of Mars surface properties, in *Mars*, edited by B. M. Jakosky et al., Univ. of Ariz. Press, Tucson.

Weeks, R. J., et al. (1996), Surface roughness, radar backscatter, and visible and near-infrared reflectance in Death Valley, California, *J. Geophys. Res.*, *101*(E10), 23,077–23,090.

———————————

A. R. Gillespie and A. Mushkin, Department of Earth and Space Sciences, Campus Box 351310, University of Washington, Seattle, WA 98195, USA. (mushkin@u.washington.edu)